# A Superlattice of Alternately Stacked Ni–Fe Hydroxide Nanosheets and Graphene for Efficient Splitting of Water

**Wei Ma,[†,‡,§] Renzhi Ma,[*,†] Chengxiang Wang,[†] Jianbo Liang,[†] Xiaohe Liu,[*,‡] Kechao Zhou,[*,‡,§] and Takayoshi Sasaki[†]**

[†]International Center for Materials Nanoarchitectonics (MANA), National Institute for Materials Science (NIMS), Namiki 1-1, Tsukuba, Ibaraki 305-0044, Japan and [‡]School of Resources Processing and Bioengineering and [§]State Key Laboratory of Powder Metallurgy, Central South University, Changsha 410083, PR China

**ABSTRACT** Cost-effective electrocatalysts based on nonprecious metals for efficient water splitting are crucial for various technological applications represented by fuel cell. Here, 3*d* transition metal layered double hydroxides (LDHs) with varied contents of Ni and Fe were successfully synthesized through a homogeneous precipitation. The exfoliated Ni–Fe LDH nanosheets were heteroassembled with graphene oxide (GO) as well as reduced graphene oxide (rGO) into superlattice-like hybrids, in which two kinds of oppositely charged nanosheets are stacked face-to-face in alternating sequence. Heterostructured composites of $Ni_{2/3}Fe_{1/3}$ LDH nanosheets and GO ($Ni_{2/3}Fe_{1/3}$-GO) exhibited an excellent oxygen evolution reaction (OER) efficiency with a small overpotential of about 0.23 V and Tafel slope of 42 mV/decade. The activity was further improved *via* the combination of $Ni_{2/3}Fe_{1/3}$ LDH nanosheets with more conductive rGO ($Ni_{2/3}Fe_{1/3}$-rGO) to achieve an overpotential as low as 0.21 V and Tafel plot of 40 mV/decade. The catalytic activity was enhanced with an increased Fe content in the bimetallic Ni–Fe system. Moreover, the composite catalysts were found to be effective for hydrogen evolution reaction. An electrolyzer cell powered by a single AA battery of 1.5 V was demonstrated by using the bifunctional catalysts.

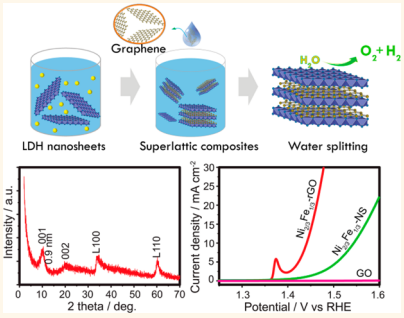


**KEYWORDS:** layered double hydroxide · graphene · heteroassembly · water splitting · nonprecious metal catalyst

The splitting of water to generate oxygen (oxygen evolution reaction, OER) and hydrogen (hydrogen evolution reaction, HER), $H_2O \rightarrow {}^1/_2O_2 + H_2$, holds an ultimate potential to cater the energy demand on a global scale and relax the current environment pollution originating from the mass consumption of fossil sources. However, the electrolysis of water, breaking the O–H bonds and forming O–O double bonds accompanied by the release of protons or electrons, is kinetically sluggish in both acidic and alkaline media, and generally requires a cell potential substantially higher than the thermodynamic value of 1.23 V, that is, a large overpotential.[1–5] Therefore, it is crucial to employ highly active catalysts to decrease the overpotential and thus realize efficient water splitting. At present, typical catalysts used in water splitting reactions are mostly based on noble metals such as Pt, Ru, Ir, and their alloys/compounds because of outstanding OER or HER activity.[6–11] Nevertheless, the scarcity and high cost of these precious metals prevent them practically being used on a large scale. Consequently, it becomes more and more urgent to exploit alternative electrocatalysts composed of nonprecious metals or earth-abundant elements that still show high catalytic capability to accelerate the reactions under reduced overpotential.[12–14] Over the past decade, considerable efforts have been shifted to the development of low-cost 3*d* transition metal hydroxides/oxides as candidate catalysts for water splitting because of their earth abundance and promising catalytic characteristics.[15–17]

Layered double hydroxide (LDH), in a general formula of $[M^{2+}_{1-x}M^{3+}_x(OH)_2]^{x+}$-$[A^{n-}_{x/n}]^{x-} \cdot mH_2O$, is a class of layered materials comprising positively charged metal hydroxide layers and charge-balancing anions between the layers.[18,19] These materials have recently attracted enormous attention as potential OER or HER catalysts when 3*d* transition metals (e.g., Fe, Co, Ni) were

* Address correspondence to MA.Renzhi@nims.go.jp, liuxh@csu.edu.cn, zhoukechao@csu.edu.cn.

Received for review December 8, 2014 and accepted January 21, 2015.

**Published online January 21, 2015**
10.1021/nn5069836

incorporated in the host layers.[20−23] Such studies have demonstrated the significance of combining heterogeneous transition metals, for example, Ni−Fe in comparison with single Ni or Fe component, to reduce the overpotential and increase OER activity.[23−27] Furthermore, by hybridizing with conductive nanocarbon, Ni−Fe hydroxide/oxide nanoplates exhibited remarkable catalytic performance and stability in the electrochemical oxidation of water, comparable to that of commercial Ir-based catalysts.[28] In particular, delamination/exfoliation of LDH can produce positively charged nanosheets with a unilamellar thickness (<1 nm) and ultimate 2-dimension (2D) anisotropy (aspect ratio >100), resulting in a superhigh specific surface area of ca. 1000 $m^2/g$ in theory.[29−31] The surface exposure of all transition metal atoms is very favorable in expediting the redox reaction due to a fast proton-coupled electron transfer process and rapid diffusion of the reactants. However, preparation of efficient catalysts based on LDH nanosheets has been restricted by their tendency to aggregate, insulating nature, and poor stability, *etc.*[32]

To overcome these issues, the heteroassembly of hydroxide nanosheets and graphene has been proposed as a new approach to achieve full potential of the two complementing 2D counterparts. In the heterostructure, graphene, with an extremely high specific surface area of about 2600 $m^2/g$ in theory and high electrical conductivity of $\sim 10^6$ S/cm, may serve as conducting paths to enhance charge transfer and mass transport during the catalytic reaction. Especially, electrostatic face-to-face stacking of positively charged LDH nanosheets and negatively charged graphene (oxide) in alternating sequence at a molecular scale enables direct interfacial contact between 3*d* transition metals and carbon, significantly shortening diffusion distance. However, there are no reports on successful synthesis of a true superlattice electrocatalyst for water splitting through direct and molecular assembly of exfoliated LDH nanosheets and graphene (oxide).

In the current work, $Ni^{2+}$−$Fe^{3+}$ LDHs with varied ratios of nickel and iron were synthesized using a homogeneous precipitation method in the presence of HMT (hexamethylenetetramine, $C_6H_{12}N_4$) and AQS (anthraquinone-2-sulfonate anions, $C_{14}H_7O_5S^-$). After exfoliation into nanosheets, they were assembled with graphene oxide (GO) into a superlattice structure, which showed outstanding OER performance in 1 M KOH aqueous solution, achieving a small overpotential of ∼0.23 V and Tafel slope of ∼42 mV/decade. It was revealed that the catalytic activity was enhanced with an increased Fe content in LDH nanosheets. When a combination of $Ni_{2/3}Fe_{1/3}$ LDH nanosheets and reduced GO (rGO) was optimized, the overpotential could be reduced to ∼0.21 V and the corresponding Tafel slope to ∼40 mV/decade. In addition, the $Ni_{2/3}Fe_{1/3}$-rGO superlattice composite was also functional in catalyzing the HER process. This enabled the construction of an electrolyzer device employing the newly developed superlattice composites as bifunctional catalysts for total water splitting under a low cell potential of 1.5 V.

## RESULTS AND DISCUSSION

$Ni^{2+}$−$Fe^{3+}$ LDHs were synthesized by refluxing a solution of $NiCl_2$−$FeCl_2$−AQS−HMT at varied Ni:Fe ratios (e.g., 2:1, 3:1, and 4:1) under the protection of nitrogen gas (see Supporting Information for details). During the homogeneous precipitation of $Ni^{2+}$−$Fe^{2+}$ hydroxide *via* a slow hydrolysis of HMT, $Fe^{2+}$ was oxidized into $Fe^{3+}$ *in situ* by AQS, forming an LDH structure intercalating $AQS^{2-}$ in the interlayer space.[33] The morphology of as-prepared $Ni_{2/3}Fe_{1/3}$ LDH was characterized by scanning electron microscopy (SEM), as shown in Figure S1a. The platelets display typical lateral size of several hundred nm, and thickness estimated to be a few tens of nm. All the AQS-intercalated LDHs exhibit a similar basal spacing of ∼2.0 nm, as evidenced by X-ray diffraction (XRD) pattern in Supporting Information, Figure S1b. The chemical composition of as-prepared platelets can be calculated as $Ni_{2/3}Fe_{1/3}(OH)_2AQS_{1/6}\cdot 0.5H_2O$ according to the results of thermogravimetric measurements (see Figure S2). Upon anion-exchange into DS (dodecyl sulfate, $C_{12}H_{25}OSO_3^-$) form, the interlayer spacing was increased to ∼2.4 nm. The interlayer expansion facilitates the subsequent delamination/exfoliation of LDH platelets into unilamellar nanosheets in formamide under mechanical shaking. As shown in Scheme 1, the LDH nanosheets were then heteroassembled with graphene (GO or rGO) *via* electrostatic flocculation to prepare hybrid catalysts for water splitting.

Figure 1a displays the atomic force microscopy (AFM) image of exfoliated $Ni_{2/3}Fe_{1/3}$ LDH nanosheets ($Ni_{2/3}Fe_{1/3}$-NS). The lateral size of the obtained nanosheets is typically a few hundred nanometers. The measured thickness is around 0.8 nm, slightly larger than the crystallographic thickness of LDH host layers (0.48 nm) due to surface absorption of water or organic molecules. The ultrathin character was further characterized by transmission electron microscopy (TEM) observation shown in Supporting Information, Figure S3. A clear Tyndall effect was observed for the collodial suspensions shown in the inset, indicating that the nanosheets are well dispersed in formamide. Similarly, Figure 1panels b and c show AFM images of GO and rGO nanosheets, respectively, with typical lateral size of a few micrometers. The chemical reduction using hydrazine ($N_2H_4\cdot H_2O$) reduced the thickness from ∼1.0 nm for GO to ∼0.5 nm for rGO nanosheets, a direct consequence of partially removing the oxygen-containing functional groups such as −OH and −COOH.[34−36] Additionally, the photographs of suspensions shown in the insets of Figure 1 panels

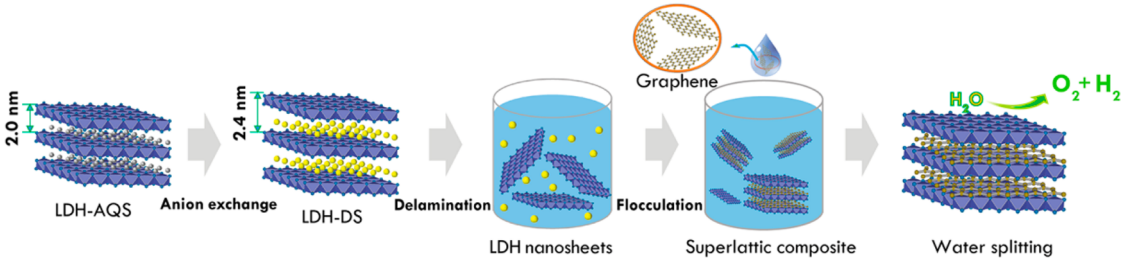


**Scheme 1. Procedures of hetero-assembling Ni−Fe LDH nanosheets and graphene for water splitting.**

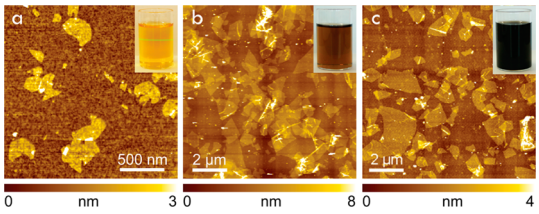


**Figure 1. AFM images of $Ni_{2/3}Fe_{1/3}$ LDH nanosheets (a), GO (b), and rGO (c) nanosheets (insets: photographs of corresponding nanosheet suspensions).**

b and c depict the corresponding color change from brown for GO into black for rGO nanosheets.

The flocculation of $Ni_{2/3}Fe_{1/3}$-NS with graphene (GO or rGO) was carried out by mixing two nanosheet suspensions in a mass ratio of ~5.13 based on a hypothetical area matching the model in Table S1 (see Supporting Information). Figure 2a,i illustrates a typical XRD pattern of $Ni_{2/3}Fe_{1/3}$-GO flocculated product with an interlayer spacing of ~1.1 nm. The value is slightly smaller than the added sum of crystallographic thicknesses consisting of LDH nanosheets (0.48 nm) and GO (0.84 nm), which may be a consequence of electrostatic attraction between oppositely charged nanosheets as well as a possible decrease in the thickness of GO nanosheets arising from a different oxidation degree.[37] The interlayer spacing further decreased to 0.9 nm for $Ni_{2/3}Fe_{1/3}$-rGO composites due to removal of oxygen-containing functional groups from original GO nanosheets (Supporting Information, Figure S4). In addition, the diffraction peaks around 35° and 60° in both XRD patterns are derived from in-plane (100) and (110) reflections of $Ni_{2/3}Fe_{1/3}$ LDH, indicating that the 2D structure of LDH nanosheets are maintained. Figure 2b shows TEM observation on the $Ni_{2/3}Fe_{1/3}$-GO composite. The morphology of thin flakes illustrates a possible scenario that LDH nanosheets adhere to GO through electrostatic interaction due to their opposite charge. As exhibited in the top-right inset of Figure 2b, the selected area electron diffraction (SAED) pattern confirms that the composite is composed of LDH and GO nanosheets. A high-resolution transmission electron microscopy (HRTEM) image given in Figure 2c further reveals a lamellar structure, in which the lamellar fringes with different contrast might be interpreted as alternately stacked LDH and GO nanosheets. Similar results on $Ni_{2/3}Fe_{1/3}$-rGO composites were also observed and shown in Supporting Information, Figure S5.

As-prepared Ni−Fe LDH nanosheets or hybrid composites were coated onto glassy carbon with a catalyst loading ~0.25 mg/cm$^2$ and used as a working electrode. The catalytic activity for the OER in 1 M KOH aqueous solution, $2OH^- \rightarrow {}^1/_2O_2 + H_2O + 4e^-$, was evaluated at a scan rate of 5 mV/s in a standard three-electrode system using Ag/AgCl as a reference electrode and coiled Pt wire as a counter electrode. During the scanning, the working electrode was continually rotated at 1600 rpm to remove generated oxygen gas and limit the diffusion effect. Figure 3a exhibits representative *iR*-corrected linear sweep voltammetry (LSV) curves of as-prepared $Ni_{2/3}Fe_{1/3}$ LDH-based catalysts as well as those with GO. In the polarization curves, the peak around 1.37 V *versus* RHE is ascribed to a possible redox reaction of $Ni^{2+}/Ni^{3+}$ in the LDH nanosheets.[38,39] It is apparent that $Ni_{2/3}Fe_{1/3}$-NS exhibit high OER activity, in stark contrast with an almost negligible response of GO nanosheets. Notably, the activity for $Ni_{2/3}Fe_{1/3}$-NS is substantially improved after hybridizing with GO. As presented in Figure 3 panels b and c, an overpotential of 0.23 V required at a current density $j$ = 10 mA/cm$^2$ for $Ni_{2/3}Fe_{1/3}$-GO composite is much smaller than that of $Ni_{2/3}Fe_{1/3}$-NS, 0.31 V. In addition, the corresponding Tafel slope of $Ni_{2/3}Fe_{1/3}$-GO, 42 mV/decade, is much superior to an original value of 76 mV/decade for $Ni_{2/3}Fe_{1/3}$-NS. The best performance can be achieved when integrating $Ni_{2/3}Fe_{1/3}$-NS with more conductive rGO into a superlattice structure. The overpotential is reduced to as low as 0.21 V, and the Tafel slope is also reduced to 40 mV/decade, outperforming most of the 3*d* transition metal hydroxide/oxide OER catalysts reported so far.[40−43] To further evaluate the electrocatalytic activity, a histogram of turnover frequency (TOF) by assuming that all the transition metal ions in the catalysts are contributing to the reaction is summarized in Figure 3d, which also confirms that $Ni_{2/3}Fe_{1/3}$-rGO composite has the highest TOF of ~0.1 s$^{-1}$ at an overpotential of 0.3 V. The improved catalytic performance for the superlattice composites is believed to be derived from the following factors. First, the incorporation of GO/rGO prevents the aggregation of LDH nanosheets and

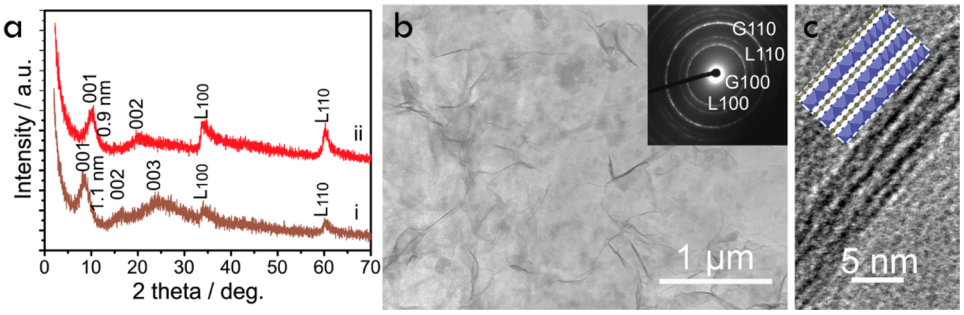


**Figure 2. (a) XRD patterns of superlattice composites of $Ni_{2/3}Fe_{1/3}$-NS and GO (i), rGO (ii). In both plots, $L_{100}$ and $L_{110}$ are in-plane diffraction peaks from the LDH nanosheet. (b) TEM image of $Ni_{2/3}Fe_{1/3}$-NS and GO composites (inset) corresponding selected area diffraction pattern, indexed to be in-plane reflections of LDH ($L_{100}$, $L_{110}$) and graphite ($G_{100}$, $G_{110}$), respectively. (c) HRTEM and schematic illustration of alternately stacked LDH nanosheets and graphene.**

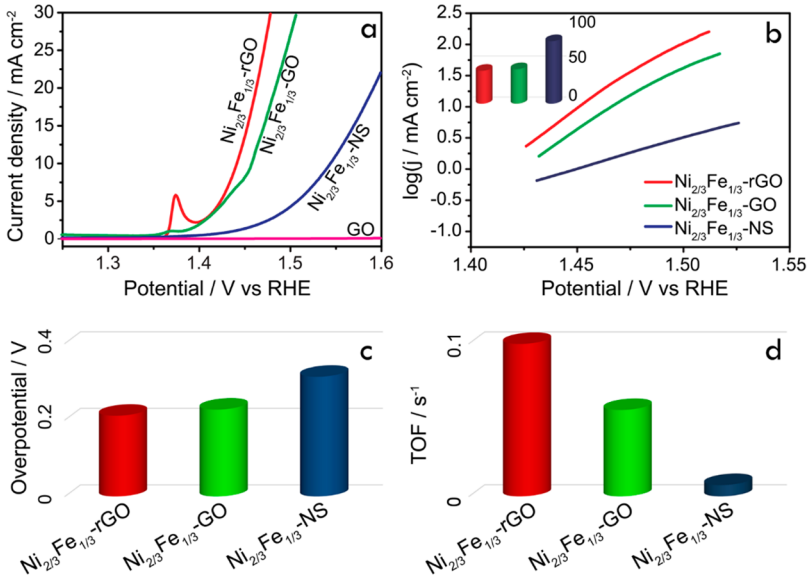


**Figure 3. (a) *iR*-corrected polarization curves of $Ni_{2/3}Fe_{1/3}$-rGO, $Ni_{2/3}Fe_{1/3}$-GO, $Ni_{2/3}Fe_{1/3}$-NS, and GO in 1 M KOH solution; (b) Tafel plots (inset: histogram of corresponding Tafel slopes); (c) overpotential required at 10 mA/cm$^2$; and (d) TOF at overpotential (0.3 V) of $Ni_{2/3}Fe_{1/3}$-rGO, $Ni_{2/3}Fe_{1/3}$-GO, and $Ni_{2/3}Fe_{1/3}$-NS.**

isolates the nanosheets, enhancing the electrochemical active surface areas (ECSA) (as shown in Supporting Information, Figure S6). Second, direct and interfacial contact between LDH nanosheets and GO/rGO at a molecular scale in the superlattices produces a synergistic effect for the OER process. Especially, LDH nanosheets may integrate with rGO more intimately due to removal of oxygen-containing functional groups from GO. The slope of Tafel plots of $Ni_{2/3}Fe_{1/3}$-rGO is also lower than that of $Ni_{2/3}Fe_{1/3}$-GO, indicating that rGO nanosheets hybridized with LDH nanosheets is most ideal for providing fast charge transport routes and largely accessible ECSA during the catalytic reaction.[44,45]

The stability and durability of as-prepared catalysts were evaluated at the current density of 5 mA/cm$^2$ and 10 mA/cm$^2$, respectively. As shown in Figure 4a, chronopotentiometric curves measured at a current density of 5 mA/cm$^2$ indicate that all the catalysts retain a nearly constant working potential, such as 1.45 V for $Ni_{2/3}Fe_{1/3}$-rGO, 1.47 V for $Ni_{2/3}Fe_{1/3}$-GO, and 1.53 V for $Ni_{2/3}Fe_{1/3}$-NS. When increasing the current density to 10 mA/cm$^2$, the initial operation potential correspondingly increases to 1.47 V for $Ni_{2/3}Fe_{1/3}$-rGO, 1.49 V for $Ni_{2/3}Fe_{1/3}$-GO, and 1.57 V for $Ni_{2/3}Fe_{1/3}$-NS, respectively. It can be clearly seen from the chronopotentiometric curves in Figure 4b that $Ni_{2/3}Fe_{1/3}$-rGO and $Ni_{2/3}Fe_{1/3}$-GO composites do not show an appreciable increase in working potential values for a prolonged testing time up to 36000 s. In contrast, the working potential of $Ni_{2/3}Fe_{1/3}$-NS is quickly increased to over 1.6 V after ~10000 s. The chronopotentiometric characterization results thus verify a much better durability of the superlattice composite catalysts than that of LDH nanosheets alone, which may be partially attributed to an enhanced mechanical strength and stability as GO/rGO serves as a supporting matrix in the composites.

The electrochemical performance of catalysts with different ratios of Ni and Fe in LDH nanosheets was investigated. As shown in Figure 5a, the current density at the same potential for $Ni_{2/3}Fe_{1/3}$-GO/rGO is generally higher than that of $Ni_{3/4}Fe_{1/4}$-GO/rGO. Furthermore,

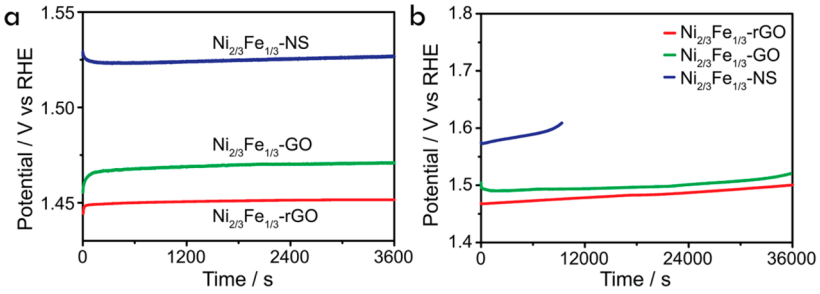


**Figure 4. Chronopotentiometry curves of $Ni_{2/3}Fe_{1/3}$-rGO, $Ni_{2/3}Fe_{1/3}$-GO, and $Ni_{2/3}Fe_{1/3}$-NS at a constant current density of 5 mA/cm$^2$ (a) and 10 mA/cm$^2$ (b), respectively.**

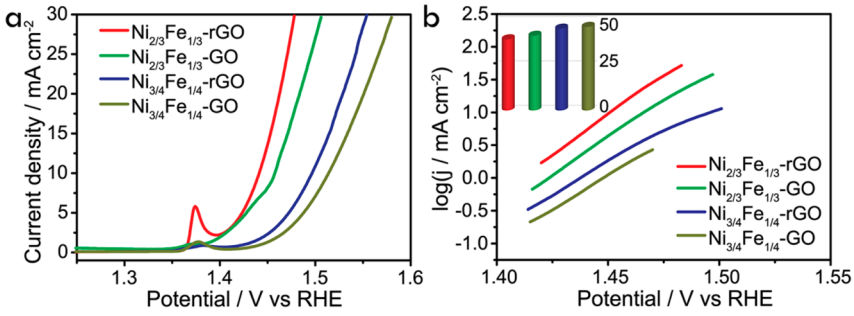


**Figure 5. *iR*-corrected polarization curves (a) and Tafel plots (b) of $Ni_{2/3}Fe_{1/3}$-rGO, $Ni_{2/3}Fe_{1/3}$-GO, $Ni_{3/4}Fe_{1/4}$-rGO, and $Ni_{3/4}Fe_{1/4}$-GO (inset: histogram of corresponding Tafel slopes).**

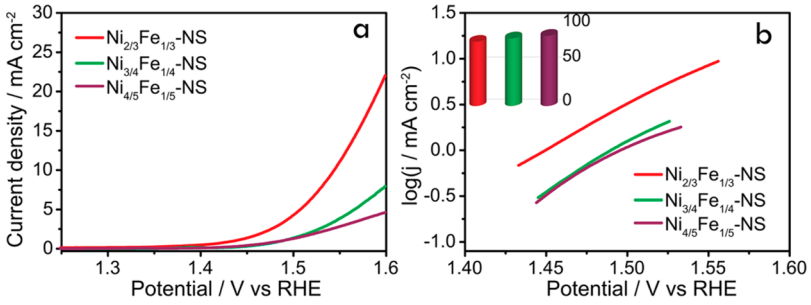


**Figure 6. *iR*-corrected polarization curves (a) and Tafel plots (b) of $Ni_{2/3}Fe_{1/3}$-NS, $Ni_{3/4}Fe_{1/4}$-NS and $Ni_{4/5}Fe_{1/5}$-NS (inset: histogram of corresponding Tafel slope).**

the curves and histogram given in Figure 5b indicate that Tafel slopes are decreased with increasing Fe content, e.g., from $Ni_{3/4}Fe_{1/4}$-rGO (46 mV/decade) to $Ni_{2/3}Fe_{1/3}$-rGO (40 mV/decade), or from $Ni_{3/4}Fe_{1/4}$-GO (47 mV/decade) to $Ni_{2/3}Fe_{1/3}$-GO (42 mV/decade). The finding that a higher Fe content in bimetallic Ni−Fe hydroxides plays a favorable role is consistent with previous reports.[46] The trends in OER reactivity for typical 3*d* transition metal elements is in the order of Fe < Co < Ni, which is governed by the bonding strength of OH-$M^{2+\delta}$ (Ni < Co < Fe).[22] It has been proposed that an increased Fe content in bimetallic Ni−Fe composites may result in partial-charge transfer from Fe sites to activate Ni centers, and enhance the catalytic activity. In addition, Fe exposed on the surface of hydroxide layers is contributing to an improved conductivity, beneficial in increasing the reaction efficiency.[47−49]

The catalytic performance of $Ni_{2/3}Fe_{1/3}$-NS, $Ni_{3/4}Fe_{1/4}$-NS, and $Ni_{4/5}Fe_{1/5}$-NS was compared, also exhibiting that higher current densities were achieved for higher Fe contents in the nanosheets (Figure 6a). As shown in Figure 6b, the Tafel slopes are decreased with increasing Fe content, for example, 82 mV/decade for $Ni_{4/5}Fe_{1/5}$-NS, 80 mV/decade for $Ni_{3/4}Fe_{1/4}$-NS, and 76 mV/decade for $Ni_{2/3}Fe_{1/3}$-NS. This again proves the positive impact of Fe content in the bimetallic catalyst. Moreover, similar trends were found for Ni−Fe hydroxide platelets intercalating AQS and DS, as shown in Supporting Information, Figure S7. The current density at the same potential increased from $Ni_{3/4}Fe_{1/4}$-DS to $Ni_{2/3}Fe_{1/3}$-DS, as well as from $Ni_{4/5}Fe_{1/5}$-AQS to $Ni_{3/4}Fe_{1/4}$-AQS and to $Ni_{2/3}Fe_{1/3}$-AQS. The reason for higher OER reactivity in DS-intercalated compounds may be derived from the expansion of interlayer gallery spacing, for example, from 2.0 to 2.4 nm, favoring the diffusion and transport of reactants, and enhancing the accessible ECSA (Figure S6b).

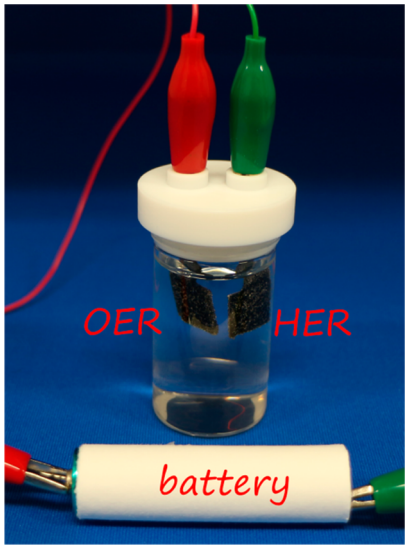


**Figure 7. Water-splitting cell driven by a 1.5 V AA battery.**

As shown in Figure S8, as-prepared $Ni_{2/3}Fe_{1/3}$-rGO superlattice composites also work for the HER reaction in 1 M KOH solution ($2\ H_2O + 2\ e^- \rightarrow 2\ OH^- + H_2$), indicating the potential of using them as bifunctional catalysts for the total splitting of water. To test the feasibility, a prototype electrolyzer cell was fabricated as displayed in Figure 7. $Ni_{2/3}Fe_{1/3}$-rGO catalysts were loaded onto two pieces of 10 mm × 10 mm nickel foams (catalyst loading ~1 mg/cm$^2$) and used as anode and cathode, respectively. Because of the remarkably small overpotential required (~0.2 V), a 1.5 V AA battery was tested to power the cell. As can be seen in Supporting Information movie, evolution of both oxygen and hydrogen gas was clearly observed. For the first time, an electrolyzer cell driven by a single AA battery unit of only 1.5 V was successfully demonstrated, generating both oxygen and hydrogen gas employing bifunctional 3*d* transition metal based catalyst.

## CONCLUSION

A homogeneous precipitation method has been employed to synthesize Ni–Fe LDHs with different contents of Ni and Fe. After exfoliation, superlattice structures of Ni–Fe LDH nanosheets and GO/rGO were successfully prepared. The electrocatalytic activity tests for the OER reaction indicate that $Ni_{2/3}Fe_{1/3}$-rGO superlattice composites exhibit the best performance, with a remarkably small overpotential of 0.21 V, and Tafel slope of 40 mV/decade. This is much better than the performance of using LDH nanosheets alone, indicating ECSA as well as the synergistic effect derived from the face-to-face interfacial hybridization of redoxable LDH nanosheets and conductive graphene at a molecular scale in the superlattice structure. It was also revealed that the catalytic activity of Ni–Fe LDH catalysts increases with the increase of Fe content, underscoring the significant role of Fe in the bimetallic catalysts. In addition, Ni–Fe-rGO superlattice composites are functional in catalyzing the HER process. As a result, a prototype electrochemical cell was successfully demonstrated by using as-prepared superlattice composites as bifunctional catalysts for both OER and HER driven by a single battery of only 1.5 V. This work offers a novel molecular-scale hybridizing strategy based on nonprecious 3*d* transition metal elements to develop bifunctional catalysts with high catalytic efficiency and high durability for potential applications in renewable energy technology such as fuel cells, *etc*.

## MATERIALS AND METHODS

**Synthesis of Ni–Fe LDH.** Ni–Fe LDHs were synthesized according to the previously reported topochemical oxidation method.[33] Yellow-colored Ni–Fe LDH platelets were obtained *via* a homogeneous precipitation procedure: 7.5 mmol of $NiCl_2 \cdot 6H_2O$ and $FeCl_2 \cdot 4H_2O$ with the Ni:Fe ratio designated at 2:1, 3:1, and 4:1, anthraquinone-2-sulfonic acid sodium salt monohydrate (AQS, 5 mmol) and hexamethylenetetramine (HMT, 60 mmol) were dissolved in 1000 mL of Milli-Q water. The solution was refluxed under continuous magnetic stirring and nitrogen gas protection for 6 h.

**Anion Exchange and Delamination of Ni–Fe LDH.** A 0.2 g sample of as-synthesized Ni–Fe LDH intercalated with AQS was dispersed into 200 mL of water/ethanol (1:1, v/v) binary solution containing 1 M sodium dodecyl sulfate (SDS, $C_{12}H_{25}OSO_3Na$) and 2 mM HCl. The suspension was shaken for 1 week to complete the exchange into the $DS^-$ form. For exfoliation, 0.02 g of Ni–Fe LDH intercalated with $DS^-$ was dispersed into 50 mL of formamide and shaken for 48 h.

**Synthesis of Graphene Oxide Nanosheets.** Graphene oxide (GO) was synthesized using a modified Hummers method.[50] Typically, 1 g of natural graphite (~100 mesh) was first heated at 500 °C for 1 h. The metal ions were removed by treating with HCl. The purified graphite was stirred in a mixed solution of $H_2SO_4$ (50 mL) and $KNO_3$ (1.2 g), and then 6 g of $KMnO_4$ was slowly added into the suspension. After 6 h, 30 mL of Milli-Q water was added, and the suspension was kept below 80 °C in a cooling bath. After another addition of 200 mL of Milli-Q water and a slow addition of 6 mL of $H_2O_2$ (30 wt %), the suspension was stirred for another hour and finally diluted into 1000 mL using water. The suspension was repeatedly decanted for several times until the pH reached 5. Then ultrasonic treatment was used to exfoliate the GO slurry in water. A brown colloidal suspension of GO nanosheets was generally obtained after ~2 h of ultrasonication.

**Chemical Reduction of the Graphene Oxide Nanosheet.** Reduced graphene oxide (rGO) was prepared using hydrazine hydrate ($N_2H_4 \cdot H_2O$) as a reducing agent. Typically, an aqueous GO suspension (1 g/L, 10 mL) and $N_2H_4 \cdot H_2O$ (8 μL) were mixed with 90 mL of formamide in a round-bottom flask. The mixed solution was heated at 80 °C under stirring for ~6 h.

**Preparation of Superlattice Composites.** According to a hypothetical area matching model (Supporting Information, Table S1), a designed volume of GO or rGO nanosheet (0.1 g/L), typically several tens of milliliters, was added drop by drop into the exfoliated LDH nanosheet suspension under continuous stirring. The flocculated product was separated by centrifugation.

**Characterization.** The phase identification of the as-prepared samples was conducted by XRD (Rigaku Ultima IV diffractometer) operated at 40 kV/40 mA with Cu Kα radiation.

The morphology and dimension of as-prepared products were characterized on a JSM-6010LA SEM. HRTEM characterizations were operated on a JEM-3000F TEM. A Seiko SPA 400 AFM was used to examine the topography of the nanosheets deposited on Si wafers.

Thermogravimetric measurements were carried out using a Thermo Plus 2 TG8120 instrument in a temperature range of room temperature to 1000 °C at a heating rate of 1 °C $min^{-1}$ under air flow.

**Electrochemical Measurements.** A 2.5 mg portion of catalyst powder was dispersed in a mixed water and propanol (1:1, v/v) solution (2.5 mL), and then 7 $\mu$L of Nafion solution (10 wt %) was added. The suspension was treated in an ultrasonic bath for 30 min to prepare a homogeneous ink. The working electrode was prepared by dripping the catalyst ink onto a glassy carbon electrode with a diameter of 3 mm (catalyst loading 0.25 $mg/cm^2$), and subsequent drying at 120 °C for 12 h.

The electrochemical measurements were conducted on a CH Instruments model 760E electrochemical workstation using 1 M KOH as an electrolyte, coiled platinum wire as a counter electrode, and Ag/AgCl electrode as a reference electrode. During the measurements, the working electrode was constantly rotated at 1600 rpm to remove generated $O_2$ and $H_2$. All LSV polarization curves were corrected with 95% *iR*-compensation. The potential was calibrated with respect to a reversible hydrogen electrode (RHE) in 1 M KOH solution. ECSA were measured by cyclic voltammetry (CV) using the same working electrodes at a potential window of 0.2−0.6 vs Ag/AgCl (1 M KOH). CV curves were obtained at different scan rates of 20, 40, 60, 80, 100, and 120 mV/s. After plotting charging current density differences ($\Delta j = j_a - j_c$ at the overpotential of 300 mV) *versus* the scan rates, the slope, twice of the double-layer capacitance $C_{dl}$, is used to represent ECSA.

The turnover frequency (TOF) value is calculated from the equation:

$$\mathrm{TOF} = \frac{JA}{4Fm}$$

where *J* is the measured current density at the overpotential of 0.3 V, *A* is the surface area of the working electrode, *F* is the Faraday constant (96485 c/mol), *m* is the number of moles of active materials loaded on the electrodes.

*Conflict of Interest:* The authors declare no competing financial interest.

*Supporting Information Available:* Typical microscopic observations, TG results, XRD, electrochemical characterizations of as-prepared samples; movie showing gas evolution in the cell. This material is available free of charge *via* the Internet at http://pubs.acs.org.

*Acknowledgment.* The work was supported in part by the World Premier International Center Initiative (WPI) on Materials Nanoarchitectonics, MEXT, Japan. R.M. acknowledges support from JSPS KAKENNHI Grant No. 24310095. X.L. acknowledges support from National Natural Science Foundation of China (51372279), Hunan Provincial Natural Science Foundation of China (13JJ1005), and Shenghua Scholar Program of Central South University.

## REFERENCES AND NOTES

1. Esswein, A. J.; Nocera, D. G. Hydrogen Production by Molecular Photocatalysis. *Chem. Rev.* **2007**, *107*, 4022–4047.
2. Strasser, P.; Koh, S.; Anniyev, T.; Greeley, J.; More, K.; Yu, C.; Liu, Z. C.; Kayas, S.; Nordlund, D.; Ogasawara, H.; *et al.* Lattice-Strain Control of the Activity in Dealloyed Core−Shell Fuel Cell Catalysts. *Nat. Chem.* **2010**, *2*, 454–460.
3. Armaroli, N.; Balzani, V. The Future of Energy Supply: Challenges and Opportunities. *Angew. Chem., Int. Ed.* **2007**, *46*, 52–66.
4. Koper, M. T. M. Thermodynamic Theory of Multi-electron Transfer Reactions: Implications for Electrocatalysis. *J. Electroanal. Chem.* **2011**, *660*, 254–260.
5. Walter, M. G.; Warren, E. L.; McKone, J. R.; Boettcher, S. W.; Mi, Q.; Santori, E. A.; Lewis, N. S. Solar Water Splitting Cells. *Chem. Rev.* **2010**, *110*, 6446–6473.
6. Greeley, J.; Stephens, I. E. L.; Bondarenko, A. S.; Johansson, T. P.; Hansen, H. A.; Jaramillo, T. F.; Rossmeis, J.; Chorkendorff, I.; Nørskov, J. K. Alloys of Platinum and Early Transition Metals as Oxygen Reduction Electrocatalysts. *Nat. Chem.* **2009**, *1*, 552–556.
7. Peng, Z. M.; Yang, H. Synthesis and Oxygen Reduction Electrocatalytic Property of Pt-on-Pd Bimetallic Heteronanostructures. *J. Am. Chem. Soc.* **2009**, *131*, 7542–7543.
8. Greer, J. R. Nanoframe Catalysts. *Science* **2014**, *343*, 1319–1320.
9. Fu, Q.; Saltsburg, H.; Flytzani, S. M. Active Nonmetallic Au and Pt Species on Ceria-Based Water-Gas Shift Catalysts. *Science* **2003**, *301*, 935–938.
10. Strmcnik, D.; Uchimura, M.; Wang, C.; Subbaraman, R.; Danilovic, N.; Vliet, D. V. D.; Paulikas, A. P.; Stamenkovic, V. R.; Markovic, N. M. Improving the Hydrogen Oxidation Reaction Rate by Promotion of Hydroxyl Adsorption. *Nat. Chem.* **2013**, *5*, 300–306.
11. Bashyam, R.; Zelenay, P. A Class of Non-precious Metal Composite Catalysts for Fuel Cells. *Nature* **2006**, *443*, 63–66.
12. Gunjakar, J. L.; Kim, T. W.; Kim, H. N.; Kim, I. Y.; Hwang, S. J. Mesoporous Layer-by-Layer Ordered Nanohybrids of Layered Double Hydroxide and Layered Metal Oxide: Highly Active Visible Light Photocatalysts with Improved Chemical Stability. *J. Am. Chem. Soc.* **2011**, *133*, 14998–15007.
13. Gasteiger, H. A.; Marković, N. M. Just a Dream-or Future Reality?. *Science* **2009**, *324*, 48–49.
14. Qu, L. T.; Liu, Y.; Baek, J. B.; Dai, L. M. Nitrogen-Doped Graphene as Efficient Metal-Free Electrocatalyst for Oxygen Reduction in Fuel Cells. *ACS Nano* **2010**, *4*, 1321–1326.
15. Zou, X.; Goswami, A.; Asefa, T. Efficient Noble Metal-Free (Electro) Catalysis of Water and Alcohol Oxidations by Zinc-Cobalt Layered Double Hydroxide. *J. Am. Chem. Soc.* **2013**, *135*, 17242–17245.
16. McCrory, C. C. L.; Jung, S.; Peters, J. C.; Jaramillo, T. F. Benchmarking Heterogeneous Electrocatalysts for the Oxygen Evolution Reaction. *J. Am. Chem. Soc.* **2013**, *135*, 16977–16987.
17. Gong, M.; Zhou, W.; Tsai, M. C.; Zhou, J. G.; Guan, M. Y.; Lin, M. C.; Zhang, B.; Hu, Y. F.; Wang, D. Y.; Yang, J.; et al. Nanoscale Nickel Oxide/Nickel Heterostructures for Active Hydrogen Evolution Electrocatalysis. *Nat. Commun.* **2014**, *5*, 4695.
18. Allmann, R. The Crystal Structure of Pyroaurite. *Acta Crystallogr. Sect. B* **1968**, *24*, 972–977.
19. Clearfield, A. Role of Ion Exchange in Solid-State Chemistry. *Chem. Rev.* **1988**, *88*, 125–148.
20. Cavani, F.; Trifirò, F.; Vaccari, A. Hydrotalcite-Type Anionic Clays: Preparation, Properties and Applications. *Catal. Today* **1991**, *11*, 173–301.
21. Abellan, G.; Coronado, E.; Marti-Gastaldo, C.; Pinilla-Cienfuegos, E.; Ribera, A. Hexagonal Nanosheets from the Exfoliation of $Ni^{2+}$−$Fe^{3+}$ LDHs: a Route Towards Layered Multifunctional Materials. *J. Mater. Chem.* **2010**, *20*, 7451–7455.
22. Subbaraman, R.; Tripkovic, D.; Chang, K. C.; Strmcnik, D.; Paulikas, A. P.; Hirunsit, P.; Chan, M.; Greeley, J.; Stamenkovic, V.; Markovic, N. M. Trends in Activity for the Water Electrolyser Reactions on 3*d* M (Ni,Co,Fe,Mn) Hydr(oxy) oxide Catalysts. *Nat. Mater.* **2012**, *11*, 550–557.
23. Lu, Z. Y.; Xu, W. W.; Zhu, W.; Yang, Q.; Lei, X. D.; Liu, J. F.; Li, Y. P.; Sun, X. M.; Duan, X. Three-Dimensional NiFe Layered Double Hydroxide Film for High-Efficiency Oxygen Evolution Reaction. *Chem. Commun.* **2014**, *50*, 6479–6482.
24. Corrigan, D. A. The Catalysis of the Oxygen Evolution Reaction by Iron Impurities in Thin Film Nickel Oxide Electrodes. *J. Electrochem. Soc.* **1987**, *134*, 377–384.
25. Miller, E. L.; Rocheleau, R. E. Electrochemical Behavior of Reactively Sputtered Iron-Doped Nickel Oxide. *J. Electrochem. Soc.* **1997**, *144*, 3072–3077.

26. Legrand, L.; Abdelmoula, M.; Géhin, A.; Chaussé, A.; Génin, J. M. R. Electrochemical Formation of a New Fe(II)−Fe(III) Hydroxy-Carbonate Green Rust: Characterisation and Morphology. *Electrochim. Acta* **2001**, *46*, 1815–1822.
27. Hickling, A.; Hill, S. Oxygen Overvoltage. Part I. The Influence of Electrode Material, Current Density, and Time in Aqueous Solution. *Discuss. Faraday Soc.* **1947**, *1*, 236–246.
28. Gong, M.; Li, Y. G.; Wang, H. L.; Liang, Y. Y.; Wu, J. Z.; Zhou, J. G.; Wang, J.; Regier, T.; Wei, F.; Dai, H. J. An Advanced Ni−Fe Layered Double Hydroxide Electrocatalyst for Water Oxidation. *J. Am. Chem. Soc.* **2013**, *135*, 8452–8455.
29. Ma, R. Z.; Liu, Z. P.; Li, L.; Iyi, N.; Sasaki, T. Exfoliating Layered Double Hydroxides in Formamide: A Method To Obtain Positively Charged Nanosheets. *J. Mater. Chem.* **2006**, *16*, 3809–3813.
30. O'Leary, S.; O'Hare, D.; Seeley, G. Delamination of Layered Double Hydroxides in Polar Monomers: New LDH−Acrylate Nanocomposites. *Chem. Commun.* **2002**, 1506–1507.
31. Adachi-Pagano, M.; Forano, C.; Besse, J. P. Delamination of Layered Double Hydroxides by Use of Surfactants. *Chem. Commun.* **2000**, 91–92.
32. Zhao, M. Q.; Zhang, Q.; Huang, J. Q.; Wei, F. Hierarchical Nanocomposites Derived from Nanocarbons and Layered Double Hydroxides—Properties, Synthesis, and Applications. *Adv. Funct. Mater.* **2012**, *22*, 675–694.
33. Lee, J. H.; O'Hare, D.; Jung, D. Y. Topochemical Oxidation of Transition Metals in Layered Double Hydroxides by Anthraquinone-2-Sulfonate. *Bull. Kor. Chem. Soc.* **2012**, *33*, 725–727.
34. Park, S.; Ruoff, R. S. Chemical Methods for the Production of Graphenes. *Nat. Nanotechnol.* **2009**, *4*, 217–224.
35. Zhao, J.; Pei, S.; Ren, W.; Gao, L.; Cheng, H. M. Efficient Preparation of Large-Area Graphene Oxide Sheets for Transparent Conductive Films. *ACS Nano* **2010**, *4*, 5245–5252.
36. Stankovich, S.; Dikin, D. A.; Piner, R. D.; Kohlhaas, K. A.; Kleinhammes, A.; Jia, Y. Y.; Nguyen, S. T.; Ruoff, R. S. Synthesis of Graphene-Based Nanosheets *via* Chemical Reduction of Exfoliated Graphite Oxide. *Carbon* **2007**, *45*, 1558–1565.
37. Ma, R. Z.; Liu, X. H.; Liang, J. B.; Bando, Y.; Sasaki, T. Molecular-Scale Heteroassembly of Redoxable Hydroxide Nanosheets and Conductive Graphene into Superlattice Composites for High-Performance Supercapacitors. *Adv. Mater.* **2014**, *26*, 4173–4178.
38. Oliva, P.; Leonardi, J.; Laurent, J. F.; Delmas, C.; Braconnier, J. J.; Figlarz, M.; Fievet, F. Review of the Structure and the Electrochemistry of Nickel Hydroxides and Oxy-Hydroxides. *J. Power Sources* **1982**, *8*, 229–255.
39. Corrigan, D. A.; Knight, S. L. Electrochemical and Spectroscopic Evidence on the Participation of Quadrivalent Nickel in the Nickel Hydroxide Redox Reaction. *J. Electrochem. Soc.* **1989**, *136*, 613–619.
40. Haber, J. A.; Cai, Y.; Jung, S.; Xiang, C. X.; Mitrovic, S.; Jin, J.; Bell, A. T.; Gregoire, J. M. Discovering Ce-Rich Oxygen Evolution Catalysts, from High Throughput Screening to Water Electrolysis. *Energy Environ. Sci.* **2014**, *7*, 682–688.
41. Li, Y. G.; Hasin, P.; Wu, Y. Y. $Ni_xCo_{3-x}O_4$ Nanowire Arrays for Electrocatalytic Oxygen Evolution. *Adv. Mater.* **2010**, *22*, 1926–1929.
42. Song, F.; Hu, X. L. Exfoliation of Layered Double Hydroxides for Enhanced Oxygen Evolution Catalysis. *Nat. Commun.* **2014**, *5*, 4477.
43. Trotochaud, L.; Ranney, J. K.; Williams, K. N.; Boettcher, S. W. Solution-Cast Metal Oxide Thin Film Electrocatalysts for Oxygen Evolution. *J. Am. Chem. Soc.* **2012**, *134*, 17253–17261.
44. Liang, Y. Y.; Li, Y. G.; Wang, H. L.; Zhou, J. G.; Wang, J.; Regier, T.; Dai, H. J. $Co_3O_4$ Nanocrystals on Graphene as a Synergistic Catalyst for Oxygen Reduction Reaction. *Nat. Mater.* **2011**, *10*, 780–786.
45. Vrubel, H.; Moehl, T.; Gratzel, M.; Hu, X. L. Revealing and Accelerating Slow Electron Transport in Amorphous Molybdenum Sulphide Particles for Hydrogen Evolution Reaction. *Chem. Commun.* **2013**, *49*, 8985–8987.
46. Louie, M. W.; Bell, A. T. An Investigation of Thin-Film Ni−Fe Oxide Catalysts for the Electrochemical Evolution of Oxygen. *J. Am. Chem. Soc.* **2013**, *135*, 12329–12337.
47. Trotochaud, L.; Young, S. L.; Ranney, J. K.; Boettcher, S. W. Nickel−Iron Oxyhydroxide Oxygen-Evolution Electrocatalysts: The Role of Intentional and Incidental Iron Incorporation. *J. Am. Chem. Soc.* **2014**, *136*, 6744–6753.
48. Mogerman, W. D. Metallurgical Nickel Analysis. *Ind. Eng. Chem.* **1952**, *44*, 971–973.
49. Corrigan, D. A.; Conell, R. S.; Fierro, C. A.; Scherson, D. A. *In Situ* Mössbauer Study of Redox Processes in a Composite Hydroxide of Iron and Nickel. *J. Phys. Chem.* **1987**, *91*, 5009–5011.
50. Hummers, W. S.; Offeman, R. E. Preparation of Graphitic Oxide. *J. Am. Chem. Soc.* **1958**, *80*, 1339–1339.